

Isogeometric analysis for parameterized LSM-based structural topology optimization

Yingjun Wang¹ · David J. Benson¹

Received: 3 August 2015 / Accepted: 12 November 2015 / Published online: 23 November 2015
© Springer-Verlag Berlin Heidelberg 2015

Abstract In this paper, we present an accurate and efficient isogeometric topology optimization method that integrates the non-uniform rational B-splines based isogeometric analysis and the parameterized level set method for minimal compliance problems. The same NURBS basis functions are used to parameterize the level set function and evaluate the objective function, and therefore the design variables are associated with the control points. The coefficient matrix that parameterizes the level set function is set up by a collocation method that uses the Greville abscissae. The zero-level set boundary is obtained from the interpolation points corresponding to the vertices of the knot spans. Numerical examples demonstrate the validity and efficiency of the proposed method.

Keywords Isogeometric analysis · NURBS · Topology optimization · Parameterization · Level set method

1 Introduction

Topology optimization (TO), a computational technique to optimally distribute material within a prescribed design domain, is becoming an efficient tool for guiding designers and engineers during the early stages of design. During the past three decades, TO has been used principally for traditional mechanics but its applications have been spreading to a wide range of other engineering domains such as fluids [16], heat transfer [24], vibration [41], electromagnetics [72] and

multiphysics [56]. Various methods have been considered to solve TO problems, and the most common methods among these are density-based, e.g., homogenization methods [1, 10, 59] and solid isotropic material with penalization (SIMP) methods [9, 52, 71]. These density-based methods use two or more phases to describe the material distribution of the design domain and usually one is a void phase representing “no material”. The material distribution typically adopts an element-wise constant method [60], where additional stabilization and filtering need to be introduced to eliminate numerical artifacts such as checkerboarding and mesh dependency [31, 57]. Besides the density-based methods, the evolutionary structural optimization (ESO) [70] and the genetic algorithm [65] etc. are also applicable to the TO.

Unlike the above methods using explicit material representation, another major class of TO methods, based on the level set method (LSM), uses an implicit description to parameterize the geometry [4, 62]. The LSM, proposed by Osher and Sethian [47] for the numerical analysis of surfaces and shapes, defines the interfaces between material phases by iso-contours of the level set function (LSF) [46, 55]. Due to the representation of the interfaces, the LSM-based TO avoids the ambiguities of intermediate material phases and the mesh dependency that usually exists in the density-based methods. At first, the LSM-based TO implemented the design optimization by solving Hamilton-Jacobi partial differential equation (PDE) that is naturally related to the shape derivative from the classical shape variational analysis [2, 4, 61, 62]. However, the Hamilton-Jacobi PDE needs to be solved explicitly in the conventional LSMs. This limits the time step size to a small value required to ensure the numerical stability for an explicit time-marching difference scheme [39] and usually requires the reinitialization of the LSF when it becomes too flat or steep [20], which decreases the efficiency of the TO.

✉ Yingjun Wang
yiw009@eng.ucsd.edu

¹ Department of Structural Engineering, University of California, La Jolla, San Diego, CA, USA

In order to overcome these shortcomings, parameterized LSMs were developed. The Hamilton-Jacobi PDE is converted into a simpler set of ordinary differential equations (ODEs) so that the Hamilton-Jacobi PDE are not solved directly. Chen et al. [17, 18] used multivariate B-splines on a uniform grid to parameterize the LSF in the TO because of the smoothness and local control properties of B-splines, but they only used the linear B-spline basis functions which actually are the same as the linear Lagrange basis functions. Wang et al. [63, 64] used radial basis functions (RBFs) as parameterized basis functions in the LSM-based TO problems. Luo et al. [38–40] further presented a parameterized LSM using compactly supported RBFs (CS-RBFs). Wei et al. [69] used the extended finite element method (XFEM) to address elements across boundaries and obtained more accurate optimal results. For a comprehensive review of the LSM-based TO, interested readers may refer to the article of van Dijk et al. [60].

In practice, most of TO methods use the conventional finite element method (FEM) [29] for the structural response analysis and sensitivity calculation. However, there are some drawbacks if the FEM is used. The first one is that the FEM requires the approximation of the design domain which disconnects the analysis from its geometric model. The second one is that the continuity is very low between neighboring elements, e.g., C^0 continuous for the displacement and discontinuous for the stress, which may influence the computational accuracy. The third one is that the efficiency will be greatly decreased when high-order elements are used, e.g., the ratio of linear Lagrange quadrilateral elements to nodes is roughly one, but for quadratic elements, it increases to four. In recent years, isogeometric analysis (IGA) [19, 28], which uses the same basis functions for the geometric and computational models, has become one of the most efficient methods to replace conventional computational methods (e.g., the FEM and the boundary element method) in the computations of a variety of domains [5, 7, 8, 12, 13, 26, 27, 67, 68]. Due to its high accuracy and high continuity, IGA may be used in TO problems to overcome the drawbacks of the traditional FEM.

The first isogeometric TO was proposed by Seo et al. [53], where the trimmed surface analysis technique [33] was employed for the structural response analysis and the sensitivity calculation, but the implementation is complicated and the computational time for the analysis may increase considerably when a large number of trim curves are used in a trimmed surface. Kumar et al. [34] used B-spline finite elements in density-based TO to obtain results that were free from checkerboard artifacts, where a penalization of the density gradient was used to smooth the density and obtain a mesh-independent solution. Dedè et al. [21] used a phase-field model for the formulation and the solution of the TO and used IGA for its geometric exactness in the

design domain and for the solution of phase field problems. Qian [51] presented a density-based TO where the design space is restricted to the B-spline space, and the B-spline space was free from checkerboards without additional filtering or penalty terms. In addition to TO problems, IGA has also been used in shape optimization problems [6, 43, 45, 50].

Both the parameterized LSM and IGA have their advantages in TO, but isogeometric parameterized LSM-based TO has never been tried. In this paper, we will present a new parameterized LSM using NURBS, and couple this LSM and IGA to obtain a new TO method that has the best characteristics of both the parameterized LSM and IGA such as high accuracy, smooth boundaries, and high efficiency for high-order elements. An outline of the remainder of this paper is as follows: In Sect. 2, the NURBS-based IGA is briefly reviewed. Sect. 3 describes the parameterized LSM-based TO that uses the NURBS basis functions to parameterize the LSF. The isogeometric LSM-based TO method is presented in Sect. 4. Thereafter numerical examples are presented in Sect. 5 to demonstrate the accuracy and efficiency of the new method. Finally, conclusions and future research are discussed in Sect. 6.

2 Summary of NURBS-based IGA

In IGA, non-uniform rational B-splines (NURBS) [48], constructed from B-splines, are commonly used for the numerical discretization. A knot vector \mathcal{E} , which consists of n spline basis functions, is a sequence of non-decreasing real numbers representing parametric coordinates of a curve:

$$\mathcal{E} = \{\xi_1, \xi_2, \dots, \xi_{n+p+1}\}, \quad (1)$$

where p is the order of the B-spline. The interval $[\xi_1, \xi_{n+p+1}]$ is called a patch, and the knot interval $[\xi_i, \xi_{i+1})$ is called a span.

Given a knot vector, the B-spline basis functions are recursively defined with the Cox-de Boor formula [14]:

for zero order ($p = 0$),

$$B_{i,p}(\xi) = \begin{cases} 1 & \text{if } \xi_i \leq \xi < \xi_{i+1}, \\ 0 & \text{otherwise,} \end{cases} \quad (2)$$

and for non-zero order ($p > 0$)

$$B_{i,p}(\xi) = \frac{\xi - \xi_i}{\xi_{i+p} - \xi_i} B_{i,p-1}(\xi) + \frac{\xi_{i+p+1} - \xi}{\xi_{i+p+1} - \xi_{i+1}} B_{i+1,p-1}(\xi). \quad (3)$$

It is observed that the B-spline basis functions constitute a partition of unity.

$$\sum_{i=1}^n B_{i,p}(\xi) = 1. \tag{4}$$

Another important property of the B-spline basis functions is that the continuity between knot spans is C^{p-k} where k is the multiplicity of the knots.

Two dimensional B-spline basis functions are constructed as tensor products,

$$B_{i,p}^{j,q}(\xi, \eta) = B_{i,p}(\xi)B_{j,q}(\eta). \tag{5}$$

$B_{i,p}(\xi)$ and $B_{j,q}(\eta)$ functions of order p and q , corresponding to knot vectors $\mathcal{E} = \{\xi_1, \xi_2, \dots, \xi_{n+p+1}\}$ and $\mathcal{H} = \{\eta_1, \eta_2, \dots, \eta_{m+q+1}\}$.

A bivariate B-spline surface is obtained as the tensor product of two B-spline curves

$$S(\xi, \eta) = \sum_{i=1}^n \sum_{j=1}^m B_{i,p}^{j,q}(\xi, \eta) \mathbf{P}_{i,j}, \tag{6}$$

where $\mathbf{P}_{i,j}$ are the control points. The patch for the surface is now the domain $[\xi_1, \xi_{n+p+1}] \times [\eta_1, \eta_{m+q+1}]$.

NURBS basis functions are obtained from B-splines by assigning a positive weight w_i to each basis function

$$N_{i,p}(\xi) = \frac{B_{i,p}(\xi)w_i}{\sum_{j=1}^n B_{j,p}(\xi)w_j}, \tag{7}$$

Two-dimensional NURBS basis functions are constructed as

$$N_{i,p}^{j,q}(\xi, \eta) = \frac{B_{i,p}(\xi)B_{j,q}(\eta)w_{i,j}}{\sum_{k=1}^n \sum_{l=1}^m B_{k,p}(\xi)B_{l,q}(\eta)w_{k,l}}, \tag{8}$$

where $w_{i,j}$ is the weight value corresponding to the tensor product $B_{i,p}(\xi)B_{j,q}(\eta)$.

A NURBS surface of order p in ξ direction and order q in η direction is a bivariate piecewise rational function of the form

$$S(\xi, \eta) = \sum_{i=1}^n \sum_{j=1}^m N_{i,p}^{j,q}(\xi, \eta) \mathbf{P}_{i,j}, \tag{9}$$

where $\mathbf{P}_{i,j}$ are the control points. If all weights are equal to 1, Eq. (9) has the same form as Eq. (6).

3 NURBS parameterized LSM-based TO

In the conventional implicit level set methods, structural boundaries are embedded into a scalar function of higher dimension as the zero level set, which leads to a level set model mathematically described by the Hamilton-Jacobi

PDE [38]. However, solving the Hamilton-Jacobi PDE is difficult and time-consuming. To solve this problem, parameterized LSMs are proposed to convert the Hamilton-Jacobi PDE into ordinary differential equations. In this section, we present a new parameterized LSM-based TO using NURBS basis functions that inherits the smoothness and local control properties of the NURBS [48].

3.1 Level set representation of optimization model

In the LSM, the structural boundary $\partial\Omega$ is implicitly embedded as the zero level set of a one-dimensional-higher LSF $\Phi(\mathbf{x}, t)$ which is Lipschitz continuous, where t is a pseudo time. The LSF $\Phi(\mathbf{x}, t)$ is defined over a reference domain $D \subset R^d$ ($d = 2$ or 3) and the level set representation of the structure is defined as

$$\begin{cases} \Phi(\mathbf{x}, t) > 0 & \forall \mathbf{x} \in \Omega \setminus \partial\Omega & \text{(inside),} \\ \Phi(\mathbf{x}, t) = 0 & \forall \mathbf{x} \in \partial\Omega \cap D & \text{(boundary),} \\ \Phi(\mathbf{x}, t) < 0 & \forall \mathbf{x} \in D \setminus \Omega & \text{(outside).} \end{cases} \tag{10}$$

Differentiating the LSF $\Phi(\mathbf{x}, t)$ with respect to the pseudo-time t , the Hamilton-Jacobi equation is obtained [38]

$$\frac{\partial \Phi(\mathbf{x}, t)}{\partial t} - v_n |\nabla \Phi(\mathbf{x}, t)| = 0, \quad \Phi(\mathbf{x}, 0) = \Phi_0(\mathbf{x}), \tag{11}$$

where the normal velocity $v_n = (\partial \mathbf{x} / \partial t) \cdot \mathbf{n}$ and the normal direction $\mathbf{n} = -\nabla \Phi / |\nabla \Phi|$, and $\Phi_0(\mathbf{x})$ is the initial LSF. The Hamilton-Jacobi PDE is solved to move the boundary in the normal direction.

However, a general analytical function for the scalar LSF is usually unknown in the conventional LSM-based TO, and therefore the PDE in Eq. (11) must be solved numerically [42]. Moreover, given the Courant–Friedrichs–Lewy (CFL) condition [23], the velocity extension and reinitialization must be handled carefully.

3.2 Parameterized LSM using NURBS basis functions

In order to avoid solving the Hamilton-Jacobi PDE directly, parameterized LSMs are introduced into the TO, and the original PDE is transformed into a set of ODEs that are simpler to solve numerically. The core idea of the parameterized LSM is to use the basis functions (note that NURBS are not interpolatory), based on a set of grid points, to represent the LSF in a parameterized mode as

$$\Phi(\mathbf{x}, t) = N(\mathbf{x})\phi(t) = \sum_i N_i(\mathbf{x})\phi_i(t), \tag{12}$$

where $\phi_i(t)$ is the i th expansion coefficient associating with the i th grid point and $N_i(\mathbf{x})$ is the corresponding basis function. It should be noted that $\phi_i(t)$ is not the LSF value but a

coefficient of the i th grid point if $N_i(\phi_j) \neq \delta_{ij}$, where δ_{ij} is Kronecker delta. After this parameterization, the LSF associated with both space and time is divided into the spatial terms $N_i(\mathbf{x})$ and the time dependent terms $\phi_i(t)$, and only the latter are updated during the optimization procedure.

Substituting Eq. (12) to Eq. (11), the Hamilton-Jacobi PDE is rewritten as

$$N(\mathbf{x})^T \frac{\partial \phi(t)}{\partial t} - v_n |(\nabla N(\mathbf{x}))^T \phi(t)| = 0, \tag{13}$$

where the v_n related to the time derivative of the expansion coefficients is expressed as

$$v_n = \frac{N(\mathbf{x})^T}{|(\nabla N(\mathbf{x}))^T \phi(t)|} \frac{\partial \phi(t)}{\partial t}. \tag{14}$$

Different interpolation functions are available for this parameterization, for example, the linear B-spline basis function used by Chen et al. [17,18], globally supported RBFs used by Wang et al. [63] and CS-RBFs proposed by Luo et al. [39,40]. However, their methods are all based on the interpolation points on the design domain, which is not suitable for the isogeometric interpolations because the control points are not necessarily in the design domain.

In order to use control points to interpolate the LSF of the design domain, a new parameterized method based on NURBS basis functions is proposed herein. Taking a problem in one dimension as an example, when the parametric coordinate ξ is introduced, Eq. (12) may be written as

$$\Phi(\mathbf{x}, t) = \Phi(\mathbf{x}(\xi), t) = \sum_i N_i(\xi) \phi_i(t). \tag{15}$$

Note that no parametric coordinates exist in the parameterization methods based on RBFs or CS-RBF where the physical coordinates are used directly. In order to briefly describe the formulations, the variable ξ and \mathbf{x} will be omitted when the omission does not influence the clarity.

In practice, the initial LSF as $\Phi(\mathbf{x}, 0)$ is known when the geometry of the initial design domain is known, but the initial expansion coefficients of the control points $\phi_i(0)$ are unknown. If the number of control points is m , the number of unknowns is also m , so there are m equations to be set up and the expansion coefficients are obtained by solving these equations. Therefore, m collocation points need to be sampled in the initial design domain to set up the equations as Eq. (12). Several methods for selecting collocation points have been proposed, e.g., the Gaussian quadrature scheme [15], the maximum basis point scheme [35] and the Greville abscissae scheme [32]. According to the comparison of Li and Qian [36], the Greville abscissae performs the best in terms of the stability and accuracy in isogeometric computations. Therefore, we also use the Greville abscissae

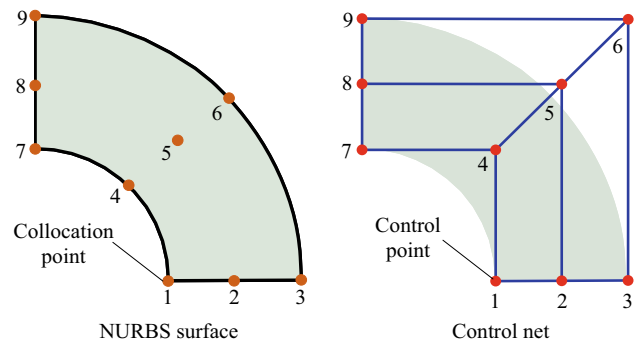


Fig. 1 An example of the Greville abscissae collocation scheme based on the surface formed from knot vectors $\mathcal{E} = \{0, 0, 0, 1, 1, 1\}$ and $\mathcal{H} = \{0, 0, 0, 1, 1, 1\}$

for the collocation points. Greville abscissae of a p -order NURBS with m control points are defined by

$$\zeta_i = \frac{1}{p} (\xi_{i+1} + \xi_{i+2} + \dots + \xi_{i+p}), \quad i = 1, 2, \dots, m, \tag{16}$$

where ξ_i is the i th knot of the knot vector $\mathcal{E} = \{\xi_1, \xi_2, \dots, \xi_{m+p+1}\}$.

For a collocation point on a NURBS surface, there are two Greville abscissae representing the coordinates in ξ and η coordinates, respectively, and $\mathbf{x}(\xi)$ and $N_i(\xi)$ should be represented as $\mathbf{x}(\xi, \eta)$ and $N_i(\xi, \eta)$. Once the Greville abscissae of the collocation points are obtained, the physical coordinates of the collocation points may be evaluated by Eq. (9), and then the LSF values of the collocation points are obtained through the LSF. Note that the collocation points and the control points have a one-to-one correspondence. An example of collocation points in a bi-quadratic surface formed from knot vectors $\mathcal{E} = \{0, 0, 0, 1, 1, 1\}$ and $\mathcal{H} = \{0, 0, 0, 1, 1, 1\}$ is shown in Fig. 1, where it can be found that each collocation point has its corresponding control point although their locations are usually different.

Applying Eq. (12) at each collocation point yields equations that may be assembled into a linear equation system

$$\Phi = A\phi, \tag{17}$$

where Φ is a vector consisting of the initial LSF values at all the collocation points, A is a matrix consisting of the NURBS basis functions values corresponding to the collocation points, and ϕ is a vector of the expansion coefficients at the control points. The expansion coefficients are obtained by solving the above equation. When the expansion coefficients are updated in the TO procedure, the new LSF values are evaluated by Eq. (17). Note that the matrix A is constant during the TO procedure. The LU factorization of A is performed only once, and each coefficient update only requires the inexpensive forward and backward substitution.

3.3 Sensitivity analysis

In the NURBS parameterized LSM-based TO, the expansion coefficients (ϕ_i in Eq. (12)) are used as the design variables instead of the LSF values in the conventional LSM-based TO. For the minimum compliance design problem, the mathematical model [63] may be defined as

$$\begin{aligned} \text{Minimize : } J(\mathbf{u}, \Phi) &= \int_{\Omega} \boldsymbol{\varepsilon}^T(\mathbf{u}) \mathbf{E} \boldsymbol{\varepsilon}(\mathbf{u}) H(\Phi) d\Omega, \\ \text{Subject to : } a(\mathbf{u}, \mathbf{v}, \Phi) &= l(\mathbf{v}, \Phi), \quad \mathbf{u}|_{\partial\Omega} = \mathbf{u}_0, \quad \forall \mathbf{v} \in \mathbf{U}, \\ V(\Omega) &= \int_{\Omega} H(\Phi) d\Omega \leq V_{\max}, \end{aligned} \tag{18}$$

where $H(\Phi)$ is the Heaviside function [61],

$$H(\Phi) = \begin{cases} 1 & \text{if } \Phi \geq 0, \\ 0 & \text{if } \Phi < 0, \end{cases} \tag{19}$$

$J(\mathbf{u}, \Phi)$ is the objective function, \mathbf{E} is the elasticity tensor and $\boldsymbol{\varepsilon}$ is the strain. The displacement is \mathbf{u} , \mathbf{u}_0 is the prescribed displacement on the admissible Dirichlet boundary and \mathbf{v} is the virtual displacement belonging to the space \mathbf{U} . The inequality $V(\Omega) \leq V_{\max}$ represents the volume constraint.

The bilinear form for the strain energy $a(\mathbf{u}, \mathbf{v}, \Phi)$ and the linear form for the load $l(\mathbf{v}, \Phi)$ may be written

$$a(\mathbf{u}, \mathbf{v}, \Phi) = \int_{\Omega} \boldsymbol{\varepsilon}^T(\mathbf{u}) \mathbf{E} \boldsymbol{\varepsilon}(\mathbf{v}) H(\Phi) d\Omega, \tag{20}$$

$$l(\mathbf{v}, \Phi) = \int_{\Omega} \mathbf{f} \mathbf{v} H(\Phi) d\Omega + \int_{\Gamma} \mathbf{p} \mathbf{v} d\Gamma, \tag{21}$$

where Ω is the material domain and Γ is the boundary, \mathbf{f} is the body force and \mathbf{p} is the boundary traction, and $H(\Phi)$ is Heaviside function whose partial derivative is the Dirac function $\delta(\Phi)$.

The original constrained optimization problem is converted into an unconstrained problem by using Lagrange multipliers

$$L(\mathbf{u}, \Phi) = J(\mathbf{u}, \Phi) + \Lambda \left[\int_{\Omega} H(\Phi) d\Omega - V_{\max} \right], \tag{22}$$

where Λ is the Lagrange multiplier. The shape derivative of Lagrangian function $L(\mathbf{u}, \Phi)$ in Eq. (22) is

$$\frac{\partial L(\mathbf{u}, \Phi)}{\partial t} = \int_{\Omega} [\Lambda - F(\mathbf{u})] \delta(\Phi) |\nabla \Phi| v_n d\Omega, \tag{23}$$

where $F(\mathbf{u}) = \boldsymbol{\varepsilon}^T(\mathbf{u}) \mathbf{E} \boldsymbol{\varepsilon}(\mathbf{u})$.

Substituting the normal velocity field v_n in Eq. (14) into Eq. (23), the derivative of Lagrangian function may be expressed as

$$\begin{aligned} \frac{\partial L(\mathbf{u}, \Phi)}{\partial t} &= \int_{\Omega} [\Lambda - F(\mathbf{u})] \delta(\Phi) N^T \frac{\partial \Phi(t)}{\partial t} d\Omega \\ &= \sum_{i=1}^m \int_{\Omega} [\Lambda - F(\mathbf{u})] \delta(\Phi) N_i \frac{\partial \phi_i(t)}{\partial t} d\Omega \\ &= \sum_{i=1}^m \int_{\Omega} -F(\mathbf{u}) \delta(\Phi) N_i \frac{\partial \phi_i(t)}{\partial t} d\Omega \\ &\quad + \Lambda \sum_{i=1}^m \int_{\Omega} \delta(\Phi) N_i \frac{\partial \phi_i(t)}{\partial t} d\Omega, \end{aligned} \tag{24}$$

where ϕ_i is the i th design variable (i.e. the expansion coefficients of the control points) and $i = 1, 2, \dots, m$ where m is the number of design variables.

Using the chain rule to differentiate the Lagrangian function Eq. (22), the shape derivative is rewritten as

$$\frac{\partial L(\mathbf{u}, \Phi)}{\partial t} = \sum_{i=1}^m \frac{\partial J(\mathbf{u}, \Phi)}{\partial \phi_i(t)} \frac{\partial \phi_i(t)}{\partial t} + \Lambda \sum_{i=1}^m \frac{\partial V(\Phi)}{\partial \phi_i(t)} \frac{\partial \phi_i(t)}{\partial t}. \tag{25}$$

Comparing Eqs. (24) and (25), the design sensitivities associating with expansion coefficients may be written as

$$\frac{\partial J(\mathbf{u}, \Phi)}{\partial \phi_i(t)} = \int_{\Omega} -F(\mathbf{u}) \delta(\Phi) N_i d\Omega, \tag{26}$$

$$\frac{\partial V(\Phi)}{\partial \phi_i(t)} = \int_{\Omega} \delta(\Phi) N_i d\Omega, \tag{27}$$

where $\delta(\Phi)$ may be defined as $\frac{1}{\pi} \frac{\gamma}{\Phi^2 + \gamma^2}$ and γ should be chosen as 2-4 times as the element size based on the numerical results in [38].

The above design sensitivities are in the domain integral form, which has the ability to create new holes in the design domain according to Luo et al. [38]. The major differences between these sensitivities and those in the conventional RBF parameterized LSM-based TO [37–39, 63] are that the expansion coefficients (i.e., design variables) ϕ_i correspond to the control points, not the nodes, and the interpolation functions N_i are the NURBS basis functions, not the RBF or CS-RBFs.

3.4 The update scheme

The optimality criteria (OC) method attempt to satisfy a set of criteria related to the behavior of the structure to solve structural optimization problems [25]. It is efficient for optimization problems with a large number of design variables and only a few constraints [11], which is exactly the case in continuous TO with a global material volume constraint. Therefore, the OC method is used here to update the design variables.

Assuming that the design variables are active, the stationary condition is that Eq. (25) equals 0, which may be also rewritten as

$$\frac{\partial L(\mathbf{u}, \Phi)}{\partial \phi_i} = \frac{\partial J(\mathbf{u}, \Phi)}{\partial \phi_i} + \Lambda \frac{\partial V(\Phi)}{\partial \phi_i} = 0. \tag{28}$$

The updating method of Luo et. al. [39] is

$$\phi_i^{(k+1)} = \left(-\frac{\partial J(\mathbf{u}, \Phi)}{\partial \phi_i^{(k)}} / \left(\Lambda^{(k)} \frac{\partial V(\Phi)}{\partial \phi_i^{(k)}} \right) \right) \phi_i^{(k)}. \tag{29}$$

In order to avoid the zero term in the denominator, a very small positive constant μ is introduced into Eq. (29),

$$D_i^{(k+1)} = D_i^{(k)} \phi_i^{(k)}, \tag{30}$$

where

$$D_i^{(k)} = -\frac{\partial J(\mathbf{u}, \Phi)}{\partial \phi_i^{(k)}} / \left(\max \left(\mu, \Lambda^{(k)} \frac{\partial V(\Phi)}{\partial \phi_i^{(k)}} \right) \right). \tag{31}$$

To implement this update method, the variable vector ϕ is normalized to a vector $\bar{\phi}$ ranging from 0 to 1, and minimal and maximal limits are set to $\bar{\phi}_{\min} = 0.0001$ and $\bar{\phi}_{\max} = 1$. The final form for the method is

$$\bar{\phi}_i^{(k+1)} = \begin{cases} \max \left\{ (1 - m) \bar{\phi}_i^{(k)}, \bar{\phi}_{\min} \right\}, & \text{if } (D_i^{(k)})^\zeta \bar{\phi}_i^{(k)} \leq \max \left\{ (1 - m) \bar{\phi}_i^{(k)}, \bar{\phi}_{\min} \right\} \\ (D_i^{(k)})^\zeta \bar{\phi}_i^{(k)}, & \text{if } \max \left\{ (1 - m) \bar{\phi}_i^{(k)}, \bar{\phi}_{\min} \right\} < (D_i^{(k)})^\zeta \bar{\phi}_i^{(k)} < \min \left\{ (1 + m) \bar{\phi}_i^{(k)}, \bar{\phi}_{\max} \right\}, \\ \min \left\{ (1 + m) \bar{\phi}_i^{(k)}, \bar{\phi}_{\max} \right\}, & \text{if } ((D_i^{(k)})^\zeta \bar{\phi}_i^{(k)}) \geq \min \left\{ (1 + m) \bar{\phi}_i^{(k)}, \bar{\phi}_{\max} \right\} \end{cases}, \tag{32}$$

where ζ ($0 < \zeta < 1$) is the damping factor and m ($0 < m < 1$) is the move limit, which are set to 0.3 and 0.05 in this paper, respectively. Note that the design variables rather than the LSFs are updated in the parameterized LSM-based TO. When the new normalized variable vector $\bar{\phi}$ is obtained, it will be rescaled to obtain the actual vector ϕ .

Another important issue is to efficiently calculate the Lagrange multiplier Λ in Eq. (31). A simple scheme to calculate the Lagrange multiplier is the bisection method, which has been successfully used in both the SIMP TO [11, 58] and the LSM-based TO [39, 66]. In the bisection method, lower and upper bounds are repeatedly calculated by an embedded loop during the iterations to satisfy the volume constraint to within a small tolerance. In order to further accelerate the calculation of Lagrange multiplier, the more efficient Ridders' method [49] is used here to replace the bisection method.

The volume constraint $F(\Lambda)$ is

$$F(\Lambda) = V(\Lambda) - V_{\max} = 0, \tag{33}$$

where $V(\Lambda)$ is volume (area for 2D problems) where the LSF value is greater than zero ($\Phi > 0$) when the Lagrange multiplier is Λ , and Λ_{\max} is maximal allowed volume as shown in Eq. (18).

Ridders' method, a root finding method, is used to find $V(\Lambda)$ satisfying the above equation as follows:

- Step 1: Set lower bound Λ_L and upper bound Λ_R of Lagrange multiplier Λ , and use Eq. (32) and the scaling method to evaluate the new variable vector ϕ_L and ϕ_R respectively, and then evaluate the total $\Phi > 0$ area (2D problem) V_L and V_R (The approach for evaluating V_0 will be discussed in Sect. 4.2.), and use Eq. 33 to obtain $F_L = F(V_L)$ and $F_R = F(V_R)$, respectively.
- Step 2: Set $\Lambda_M = 1/2(\Lambda_L + \Lambda_R)$, and evaluate the $\Phi > 0$ area V_M and use Eq. 33 to obtain $F_M = F(V_M)$.
- Step 3: Evaluate a new Lagrange multiplier Λ^* by

$$\Lambda^* = \Lambda_M + (\Lambda_M - \Lambda_L) \frac{\text{sign}(F_L - F_R) F_M}{\sqrt{F_M^2 - F_L F_R}}, \tag{34}$$

and use Eq. (32) and the scaling method to evaluate the a variable vector ϕ^* , and then evaluate the total $\Phi > 0$ area V^* and corresponding $F^* = F(V^*)$.

- Step 4: Update bounds of Lagrange multiplier:

If $F^* == 0$ then stop updating;
else if $(F_M \cdot F^* < 0)$ and $(\Lambda_M < \Lambda^*)$ then $\Lambda_L = \Lambda_M$, $F_L = F_M$, $\Lambda_R = \Lambda_{V^*}$ and $F_R = F^*$;
else if $(F_M \cdot F^* < 0)$ and $(\Lambda_M > \Lambda^*)$ then $\Lambda_R = \Lambda_M$, $F_R = F_M$, $\Lambda_L = \Lambda_{V^*}$ and $F_L = F^*$;
else if $(F_L \cdot F^* < 0)$ then $\Lambda_R = \Lambda_{V^*}$ and $F_R = F^*$;
else $\Lambda_L = \Lambda_{V^*}$ and $F_L = F^*$.

- Step 5: Repeat Step 2 to Step 4 until $|F_L| < tol$ or $|F_R| < tol$, where tol is a small number such as 10^{-5} , and V^* is the Lagrange multiplier that satisfies Eq. (33) and ϕ^* is the updated variable vector.

After the completion of the update procedure, one iteration of the TO is completed, and the new objective function value J_{new} is computed. When the relative difference of the objective function value between two iterations is less than a small number such as 0.0001, the iterative solution can be stopped and the optimal result is obtained.

4 IGA for the parameterized level set based TO

4.1 Spatial discretization

In the conventional TO, the FEM is commonly used for the sensitivity analysis, discretizing the design domain Ω into elements. The error of this discretization may lead to accuracy problems [28]. In this work, the exact NURBS geometric model created by the TO is used for the sensitivity analysis by using isogeometric analysis (IGA). Therefore, no spatial discretization error is introduced in the analysis of the TO.

One of the major differences between IGA and the conventional FEM is that the coefficients of the basis functions are referred to control points instead of nodes, and the NURBS basis functions are not interpolatory like the Lagrangian FEM basis functions. A variable value x (e.g., coordinate, displacement, or force) corresponding to a point with the geometric

parametric coordinate (ξ, η) is evaluated from the control point values

$$x(\xi, \eta) = \sum_A N_A(\xi, \eta)x_A, \tag{35}$$

where N_A is the basis function of the A th control point of the control points that influence on (ξ, η) , and x_A is the corresponding value of the control point.

The spatial discretization of the different schemes is shown Fig. 2, with a patch containing 3×3 elements. When linear elements ($p = 1$) are used, the NURBS elements are the same as the Lagrange elements, and the control points coincide with the 16 nodes of the FEM. For quadratic elements ($p = 2$), the number of nodes increases to 49 but the number of control points is only 25. This proves that the increase of degrees of freedom (DOFs) is much lower in IGA

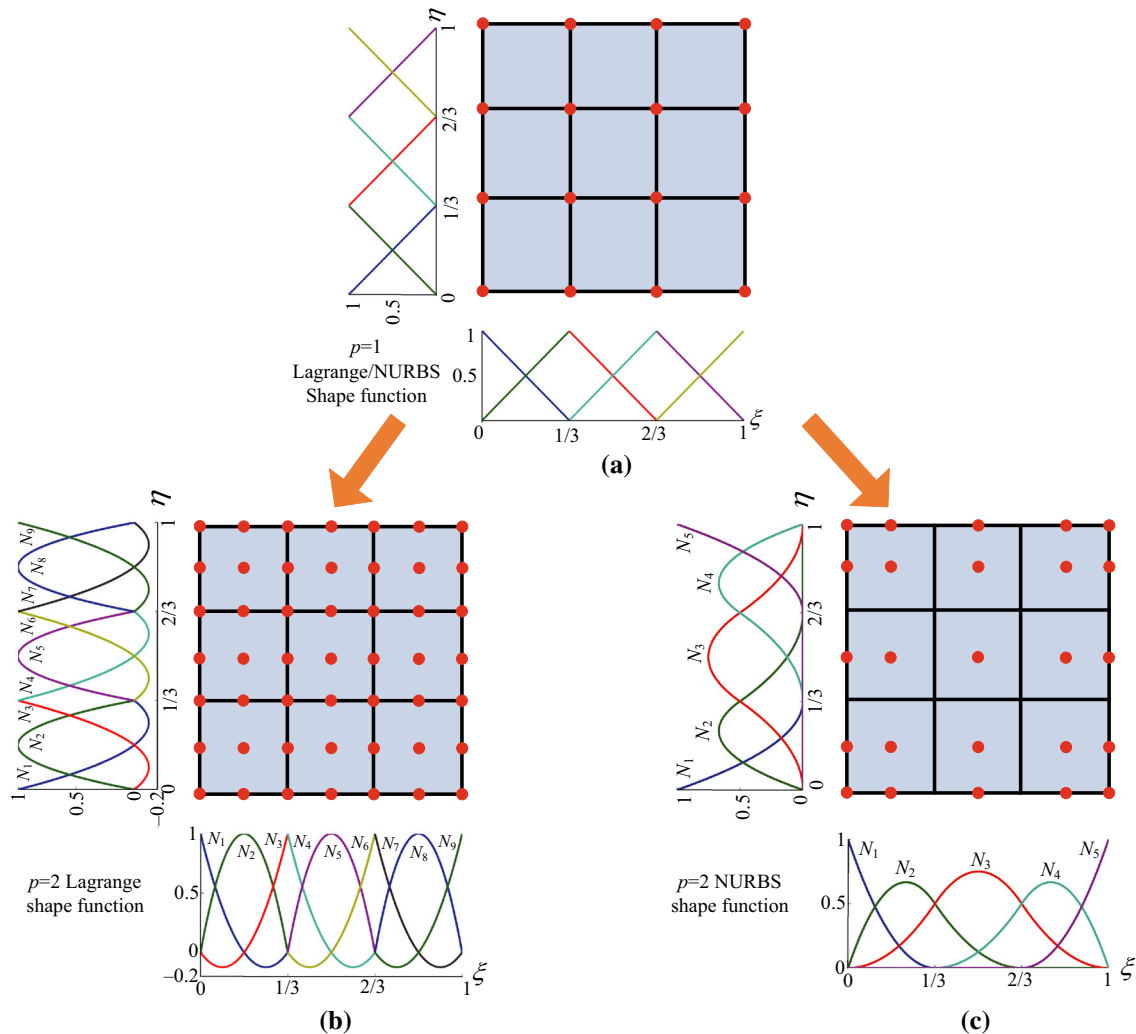


Fig. 2 Spatial discretization of FEM and IGA for a 1×1 single-patch surface model: **a** linear NURBS/Lagrange elements, **b** quadratic Lagrange elements and **c** quadratic NURBS elements

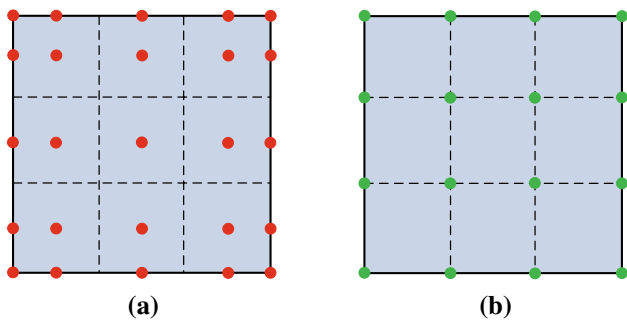


Fig. 3 Control points and interpolation points of the single-patch surface model in Fig. 2 ($p = 2$): **a** control points and **b** interpolation points

when the elements are elevated to higher order. In IGA, the control points influencing an element are not necessarily in the element domain and may be out of the problem domain. Additionally, the continuity between the quadratic NURBS elements is C^1 (see Fig. 2c) but the continuity is always C^0 between the Lagrange elements (see Fig. 2b).

4.2 Interpolation points for LSF

In Sect. 3.4, the interior of the structure is defined as the area where the LSF value is greater than zero, and it needs to be evaluated in the update procedure for the design variables. The visualization of the optimal result also requires the LSF of the design domain. In order to track the zero-level set boundaries and perform the visualization, interpolation points in the design domain need to be sampled and the LSF

values of the points need to be obtained. Using the LSF values of the interpolation points, the zero-level set boundaries and the geometry of the optimal structure are obtained by interpolation methods.

In this work, we use the vertices of the NURBS spans (i.e. elements in IGA) as interpolation points, which are the same as the nodes for linear elements. The physical coordinates of the points are available by the point inversion (projection) algorithm [48], so no meshing is needed. Now, there are two set of points: (1) control points and (2) interpolation points. Figure 3 shows the control points and interpolation points of the patch model ($p = 2$) in Fig. 2. It should be noted that the collocation points are independent of the element order in this method. Therefore, when the element order is changed, the control points are changed accordingly, but the interpolation points are still the original ones. This is not strictly necessary, but was done to simplify the implementation of the research.

The LSF values of the interpolation points may be obtained by Eq. (17) with matrix A replaced with a new matrix B that consists of the NURBS basis functions corresponding to the interpolation points. It should be noted that matrix B is a $m \times n$ matrix where m is the number of interpolation points and n is the number of control points. When the LSF values are known, the zero-level set boundaries and the area where LSF value is greater than zero are obtained by interpolation.

There usually are not multiple zero-level set boundaries that cross the same element if the mesh is sufficiently refined. According to the LSF values of the vertices, the elements may be divided into five types as shown in Fig. 4. An empty ele-

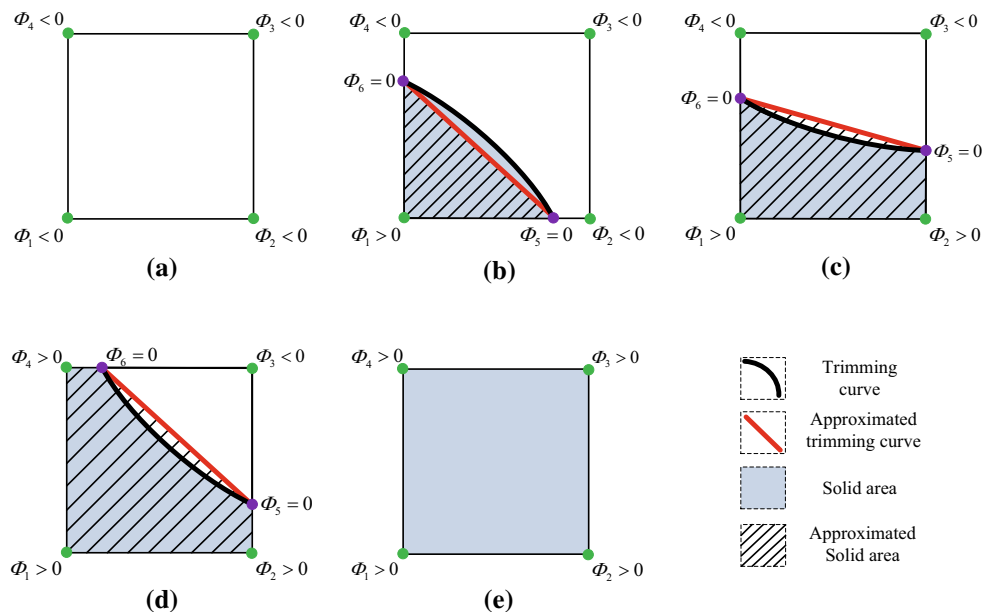


Fig. 4 Different types of elements in terms of the vertices: **a** empty element with 4 negative LSF vertices, **b** trimmed element with 1 positive LSF vertex, **c** trimmed element with 2 positive LSF vertices, **d** trimmed element with 3 positive LSF vertices and **(e)** solid element with 4 positive LSF vertices

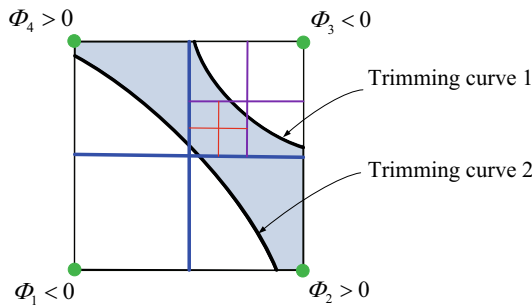


Fig. 5 Adaptive hierarchical refinement approach for an element where multiple zero-level set boundaries cross

ment is an element where the LSF values of all the vertices are less than zero (Fig. 4a), and a solid element is an element where the LSF values of all the vertices are greater than zero (Fig. 4e), and trimmed elements are classified into three types in terms of the number of vertices with a positive LSF value (Fig. 4b–d). In the case that multiple zero-level set boundaries cross an element, an adaptive hierarchical refinement approach as Fig. 5 may be used to refine the element into subelements that belongs to the five types in Fig. 4. Note that the zero-level set boundary may be regarded as a trimming curve that trims the element into solid and empty regions.

If the sign of the LSF values are different at the vertices of an element edge, linear interpolation is used to find the zero-level set point on that edge (see the purple points in Fig. 4b–d), and then the line connecting the two zero-level set points approximates the trimming curve. All the zero-level set boundaries are found after implementing the above linear interpolation for all the trimmed elements.

For the trimmed elements, the area ($\Phi > 0$) is computed by evaluating the triangular or trapezoidal area (approximated solid area in Fig. 4b–d) in the parametric space and mapping it to the physical space. When the trimming curve is not straight, this area is not exactly equal to the actual area ($\Phi > 0$). When the mesh is sufficiently refined, however, the element area error is very small, and since the trimmed elements are only a small fraction of the total, the total area error may be ignored.

4.3 Isogeometric analysis

The minimum compliance design of 2D linear elasticity problems is solved by the isogeometric TO method. The discrete equilibrium equation may be written as [29]

$$K\mathbf{u} = \mathbf{f}, \tag{36}$$

in which K is the stiffness matrix, \mathbf{u} is the displacement vector and \mathbf{f} is the external force vector associated with the control points. The stiffness matrix K consists of the element stiffness matrix K_e that is written as

$$\begin{aligned} K_e &= \int_{\Omega_e} \mathbf{B}^T \mathbf{D} \mathbf{B} d\Omega \\ &= \int_{\widehat{\Omega}_e} \mathbf{B}^T \mathbf{D} \mathbf{B} |\mathbf{J}_1| d\widehat{\Omega} \\ &= \int_{\overline{\Omega}_e} \mathbf{B}^T \mathbf{D} \mathbf{B} |\mathbf{J}_1| |\mathbf{J}_2| d\overline{\Omega} \end{aligned} \tag{37}$$

where \mathbf{B} is the strain-displacement matrix and \mathbf{D} is the stress-strain matrix, Ω_e is the domain of the element, $\widehat{\Omega}_e$ is the corresponding domain in the NURBS parametric space $\{\xi, \eta\}$, and $\overline{\Omega}_e$ is integration domain in the integration parametric space $\{\bar{\xi}, \bar{\eta}\}$. Jacobian \mathbf{J}_1 and \mathbf{J}_2 indicate the transformation relation from the NURBS parametric space to the physical space and the integration parametric space to the NURBS parametric space, respectively.

For 2D plane stress problems, the strain-displacement matrix \mathbf{B} is written as

$$\mathbf{B} = \begin{bmatrix} \frac{\partial N_1}{\partial x} & 0 & \dots & \frac{\partial N_{ne}}{\partial x} & 0 \\ 0 & \frac{\partial N_1}{\partial y} & \dots & 0 & \frac{\partial N_{ne}}{\partial y} \\ \frac{\partial N_1}{\partial y} & \frac{\partial N_1}{\partial x} & \dots & \frac{\partial N_{ne}}{\partial y} & \frac{\partial N_{ne}}{\partial x} \end{bmatrix}, \tag{38}$$

and

$$\begin{bmatrix} \frac{\partial N_i}{\partial x} & \frac{\partial N_i}{\partial y} \end{bmatrix} = \begin{bmatrix} \frac{\partial N_i}{\partial \xi} & \frac{\partial N_i}{\partial \eta} \end{bmatrix} \mathbf{J}_1^{-1}, \tag{39}$$

where N_i is a basis function of the NURBS surface and the Jacobian \mathbf{J}_1 is

$$\mathbf{J}_1 = \begin{bmatrix} \frac{\partial x}{\partial \xi} & \frac{\partial y}{\partial \xi} \\ \frac{\partial x}{\partial \eta} & \frac{\partial y}{\partial \eta} \end{bmatrix}. \tag{40}$$

The stress-strain matrix \mathbf{D} is

$$\mathbf{D} = \frac{E}{1 - \nu^2} \begin{bmatrix} 1 & \nu & 0 \\ \nu & 1 & 0 \\ 0 & 0 & \frac{1-\nu}{2} \end{bmatrix}, \tag{41}$$

where E is elastic modulus and ν is Poisson’s ratio.

The linear transformation from the Gauss quadrature domain to the NURBS parametric domain $[\xi_i, \xi_{i+1}] \times [\eta_j, \eta_{j+1}]$ is given by

$$\begin{cases} \xi = \frac{\xi_{i+1} - \xi_i}{2} (\bar{\xi} - 1) + \xi_i, \\ \eta = \frac{\eta_{j+1} - \eta_j}{2} (\bar{\eta} - 1) + \eta_j. \end{cases} \tag{42}$$

Therefore, the Jacobian \mathbf{J}_2 may be written as

$$\mathbf{J}_2 = \begin{bmatrix} \frac{\partial \xi}{\partial \bar{\xi}} & \frac{\partial \eta}{\partial \bar{\xi}} \\ \frac{\partial \xi}{\partial \bar{\eta}} & \frac{\partial \eta}{\partial \bar{\eta}} \end{bmatrix} = \begin{bmatrix} \frac{\xi_{i+1} - \xi_i}{2} & 0 \\ 0 & \frac{\eta_{j+1} - \eta_j}{2} \end{bmatrix}. \tag{43}$$

Since the elements are fixed without remeshing in the optimization procedure, in order to ensure the equation system

is nonsingular, the density based FEM [4,9,61], known as “ersatz material” approach, is employed. In this approach, the void domain is filled with a weak material having a very small elastic modulus E_w , where $E_w < 0.001 E_s$ in general. The material filling density is

$$\rho(\Phi) = \frac{(E_s - E_w)H(\Phi) + E_w}{E_s}, \quad (44)$$

where $H(\Phi)$ is the Heaviside function as Eq. (19).

When this density-based FEM is used in the numerical implementation, the element stiffness matrix is

$$\mathbf{K}'_e = \int_{\Omega_e} \mathbf{B}^T \mathbf{D} \mathbf{B} |J_1| |J_2| \rho(\Phi) d\bar{\Omega} = \mathbf{K}_e \cdot \rho_e, \quad (45)$$

where \mathbf{K}_e is the stiffness matrix of a completely solid element defined in Eq. (37), and ρ_e is material filling density of element e .

4.4 Implementation

The implementation of the isogeometric parameterized LSM-based TO is summarized in Fig. 6. The primary differences from the conventional parameterized LSM-based TO using the FEM are associated with the patch refinement and the objective function computation as discussed in the previous sections.

Each iteration starts with the design from the previous iteration. To construct an initial design for the first iteration, holes are introduced into the design domain. If the number of initial holes is too small to describe all admissible shapes, the optimal result may not be obtained by using the boundary integration scheme [39] to evaluate the design sensitivities. Even though the domain integration scheme Eq. (26) and (27) is used, too few holes may be unavailable to obtain the optimal result when the terminal criterion is satisfied as discussed in Sect. 5.1.1. Different hole initializations may also lead to different convergence rates. Therefore, equally spaced holes are usually introduced into the initial domain to efficiently obtain the optimal results [39,62].

5 Numerical examples

Numerical examples of minimal compliance design problems are presented to demonstrate the characteristics of the isogeometric LSM-based TO. The domain integration scheme defined by Eqs. (26) and (27) is used to evaluate the design sensitivities. All the examples are run on a desktop: the CPU is an Intel core i7 960 3.2GHz, the RAM is 12GB, the OS is Linux Ubuntu 12.04, and the software environment is MATLAB 2014b. The 3×3 Gauss quadrature rule is used

for the quadratic isogeometric elements used in the examples. In the “ersatz material” approach, the elastic modulus for the solid material is 1.0 and for the weak material, 0.0001. The Poisson’s ratio is 0.3. The terminal criterion is the relative difference of the objective function values between two iterations, which is set to 0.0001.

5.1 Cantilever beam

The cantilever beam, as a benchmark problem, is commonly used to evaluate TO methods [3,37–39,54,70]. The design domain of the cantilever beam is shown in Fig. 7a. The left side is fixed and a concentrated force is vertically loaded at the center point of the right side. The volume ratio, i.e., material usage ratio, is limited to 0.5 and the distribution of initial holes is shown in Fig. 7b, which are same as that used by other researchers[38,39].

5.1.1 Influence of the initial hole distribution

In the LSM-based TO, the initial holes can split to form multiple holes, or merge with other holes to form a single one, and their boundaries define the geometry of the TO result. Therefore, the distribution of the initial holes may influence the convergence rate and the geometric shape of the result. For this example, we refine the design domain (Fig. 7a) into a mesh of 64×32 quadratic 2D NURBS elements, and the influence of initial holes is explored by using different initial hole distributions as shown in Fig. 8. The radius of all the holes is 0.1.

When the mesh of 64×32 quadratic elements is used, no control point is located at the center point of the right edge (see the example in Fig. 11), so the force cannot be exactly added at a control point. An approach to address this problem is as follows: (1) find the parametric coordinates of the point where the force is added, e.g. (ξ, η) , (2) evaluate all of the basis functions $N_A(\xi, \eta)$, $A = 1, \dots, n$ at the parametric coordinates, and (3) add the force $N_A(\xi, \eta)F$ at each corresponding control point. This approach will be applied in the following examples when the load cannot be added exactly.

The number of iterations and the TO results corresponding to Fig. 8 are shown in Fig. 9. From Fig. 9a, b and c, it can be observed that the proposed method is able to automatically nucleate new holes in the material domain, and the number of iterations decreases when an initial hole approaches the loading position since the geometric changes prefer to occur along the boundaries. When the design domain is initialized with a certain number of holes and their distribution is reasonable (Fig. 9d–f), the widely accepted optimal solution [4,39] is obtained, but the number of initial holes influences the convergence speed as shown in Fig. 8f > Fig. 8e > Fig. 8d. The equal-interval hole distribution, applied throughout the domain, performs the best, which is in agreement with other

Fig. 6 The procedure flowchart of the isogeometric parameterized LSM-based TO

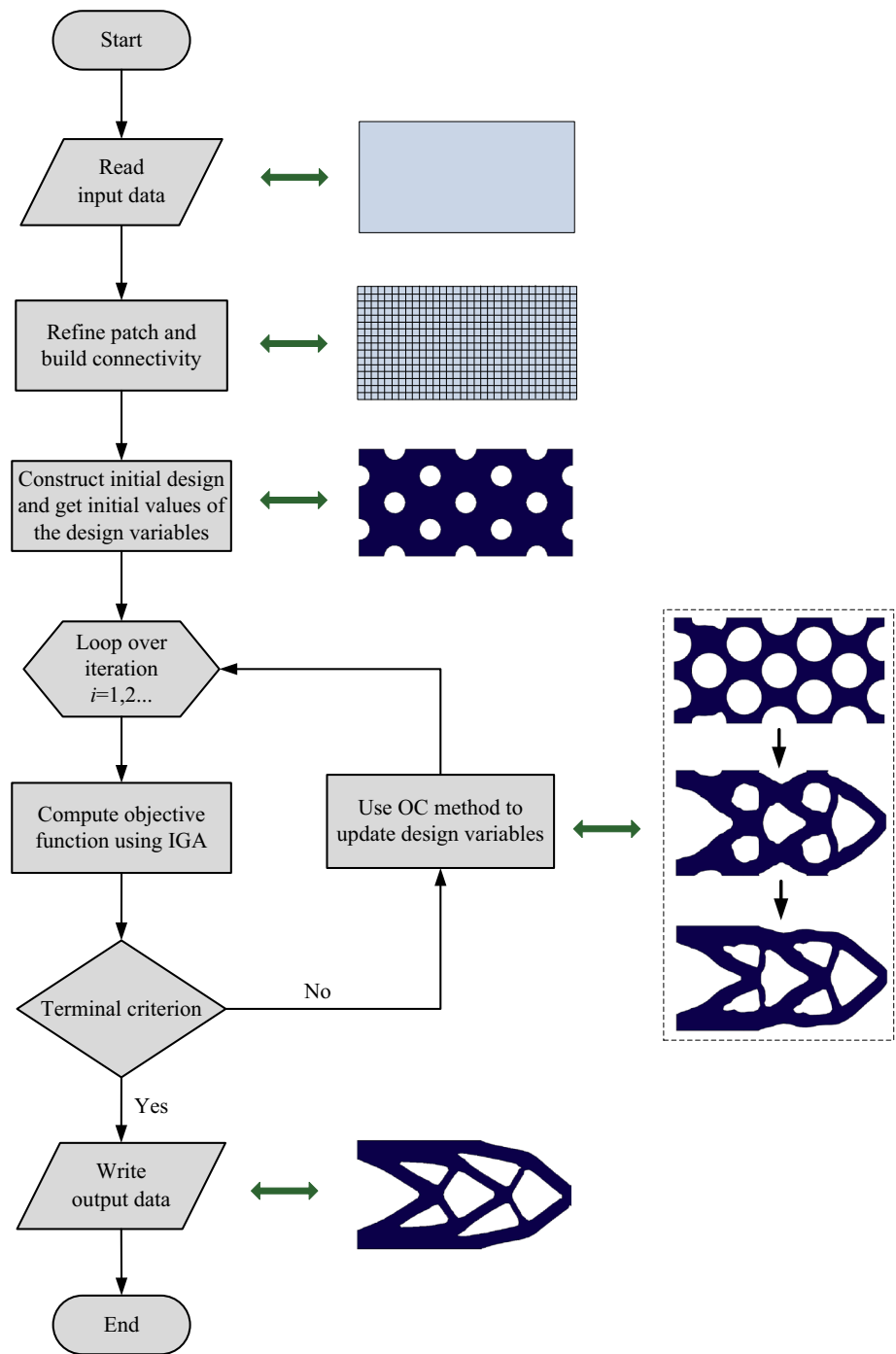
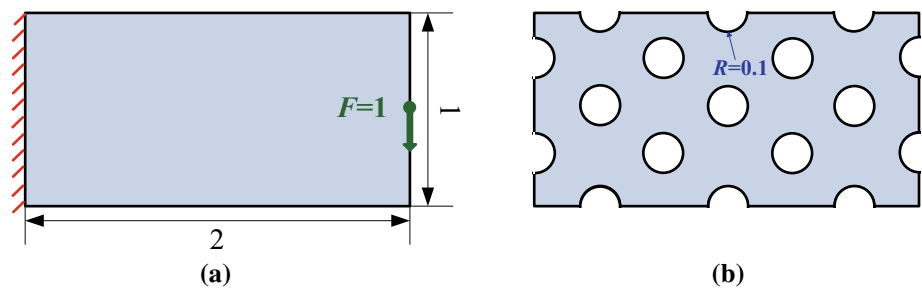


Fig. 7 Design domain and initial holes of the cantilever beam: **a** design domain and **b** distribution of initial holes



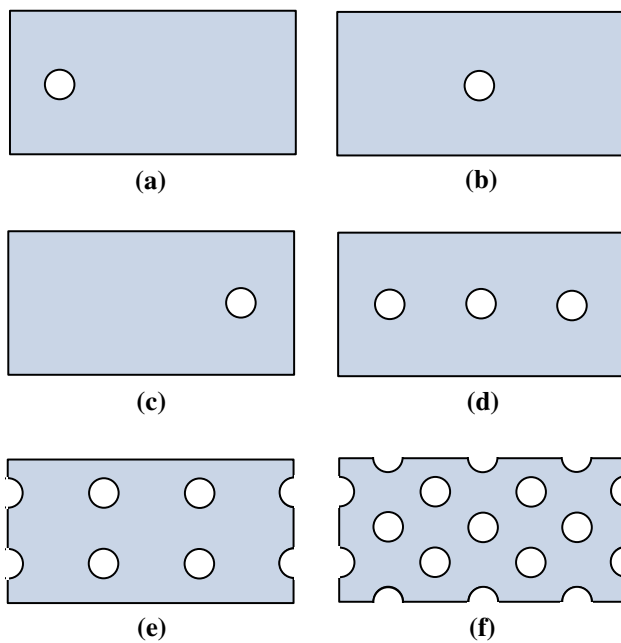


Fig. 8 Different distribution schemes of initial holes: **a** 1 left hole, **b** 1 center hole, **c** 1 right hole, **d** 3 horizontal holes, **e** 4×2 holes and **f** 17 equal-interval holes

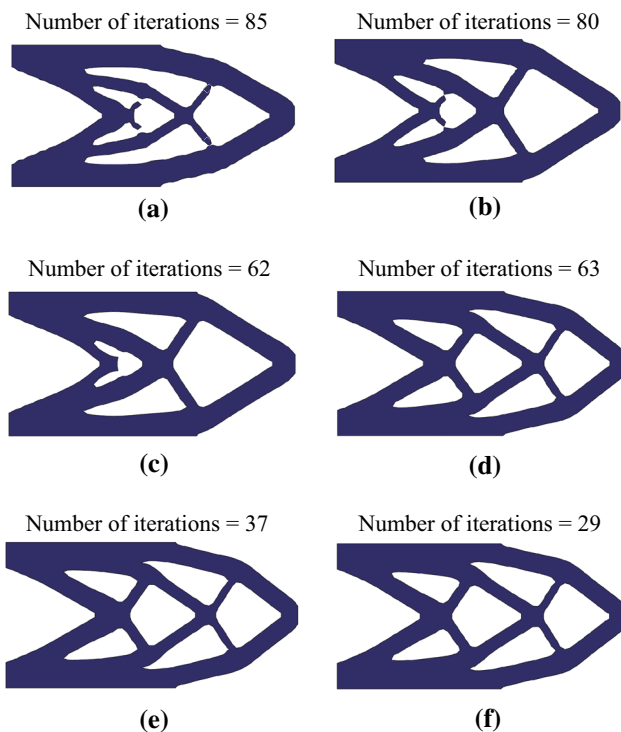


Fig. 9 The TO results of different initial holes in Fig. 8: **a** 1 left hole, **b** 1 center hole, **c** 1 right hole, **d** 3 horizontal holes, **e** 4×2 holes and **f** 17 equal-interval holes

researchers [4,38,39]. Comparing Fig. 9a–c with d–f, one initial hole is not sufficient to obtain the optimal structure when the terminal criterion is satisfied. Note that one initial

hole may produce the optimal structure if a smaller terminal criterion is set, but it will greatly increase the number of iterations.

5.1.2 IGA versus FEM

Compared to the conventional FEM, one of the biggest advantages of IGA is its high efficiency of its high-order elements. As shown in Fig. 2, the number of DOFs of IGA scheme is much less than that of the FEM. When the number of elements ($e_1 \times e_2$) is known, the DOFs of IGA (N_{IGA}) and the FEM (N_{FEM}) using quadratic elements are

$$N_{IGA} = 2(e_1 + 2)(e_2 + 2), \quad (46)$$

and

$$N_{FEM} = 2(2e_1 + 1)(2e_2 + 1). \quad (47)$$

When e_1 and e_2 are large enough, the ratio N_{IGA}/N_{FEM} is approximately $1/4$.

Mesheres of 16×8 , 32×16 , 64×32 , 128×64 and 256×128 quadratic elements are used with IGA and the FEM to compare the TO results. Figure 10 shows the optimization results with different meshes, where N.A. is “not available” when the terminal criterion could not be satisfied after hundreds of iterations. When the mesh is too coarse, e.g., 16×8 and 32×16 , the elements cannot represent the optimal structure, and therefore rough, non-optimal structures are obtained (see Fig. 10a–d).

The number of iterations increases with the mesh refinement, and the number of iterations for IGA is smaller than for the FEM. The primary reason for this is that the number of iterations is a function of the number of DOFs and that number is much smaller for IGA than the FEM for the same mesh (Fig. 2).

In order to discuss the efficiency of IGA and the FEM (using Lagrange elements) in detail, the computational time of one iteration is given in Table 1. The rate of N_{IGA}/N_{FEM} is approximately $1/4$, which confirms the estimates from Eqs. (46) and (47). The speedup of IGA/FEM ranges from 3.04 to 4.13, demonstrating the high efficiency of the proposed isogeometric TO. Note that the computational time and the number of DOFs are not proportional since the computational costs of the FEM and IGA is not linear with the DOFs, and some computations in the iteration are independent of the FEM or IGA.

5.2 Michell type structure

Another benchmark example used to evaluate the result of TO is the Michell structure problem, which is described in detail in [38,63,66,70]. In Fig. 12a, the Michell structure is

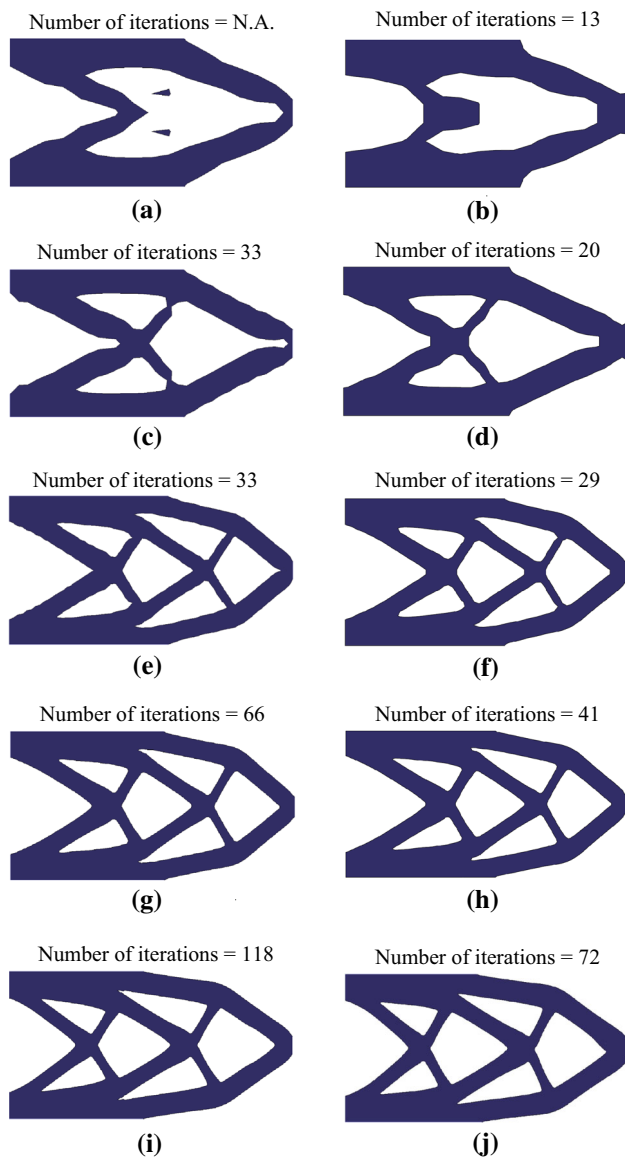


Fig. 10 The TO results of the FEM and IGA with different meshes: **a** FEM with mesh 16×8 , **b** IGA with mesh 16×8 , **c** FEM with mesh 32×16 , **d** IGA with mesh 32×16 , **e** FEM with mesh 64×32 , **f** IGA with mesh 64×32 , **g** FEM with mesh 128×64 , **h** IGA with mesh 128×64 , **i** FEM with mesh 256×128 and **j** IGA with mesh 256×128

subject to a vertical force at the middle of the bottom side. A fixed constraint is applied at the bottom-left corner and a roller constraint at the bottom-right corner. A mesh of 64×32 quadratic elements is used, and the volume ratio is set to 0.45 which is the same as that in [38].

Some selected iterations of the optimization solution are shown in Fig. 12. The structure changes rapidly during the initial iterations (Fig. 12a–c), and after the major structural features are formed (as Fig. 12d), most of the iterations will be spent in the adjustment of geometric details until the optimal structure is obtained (see Fig. 12d–f). The final result

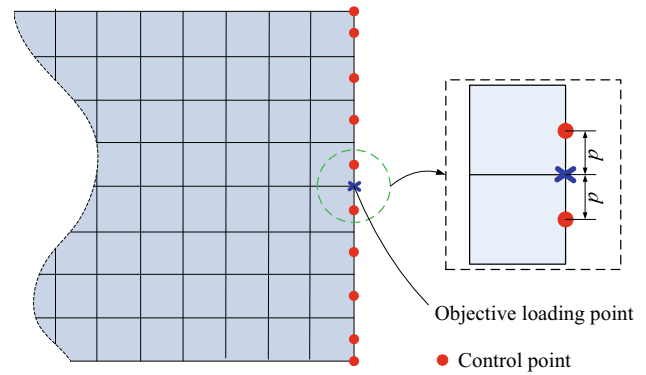


Fig. 11 An example of the inaccurate loading problem

Table 1 Efficiency comparison between IGA and the FEM by the computational time of one iteration

Cases	N_{FEM}	N_{IGA}	FEM time (s)	IGA time (s)	Speedups (IGA/FEM)
16×8	1122	360	0.62	0.20	3.10
32×16	4290	1224	2.62	0.83	3.16
64×32	18,354	4488	13.30	4.11	3.23
128×64	69,426	17,160	101.88	33.50	3.04
256×128	269,874	67,080	1489.36	360.22	4.13

is almost the same as that in reference [38] and the spokes are more uniform, which demonstrates the validity of the proposed isogeometric TO method in this paper (Fig. 13).

The objective function and the volume ratio over the iterations are shown in Fig. 14. The objective function value is very large during the initial iterations. This is a consequence of using the “ersatz material” approach for this problem. The bottom-left and bottom-right corners of the design domain (where the constraints are added) is initialized with the weak material (initial holes), resulting in large displacements and a large strain energy. The holes at the corners are rapidly filled with solid material and the objective function value decreases to normal (see the structure in Fig. 12c), which does not influence the final optimization results.

5.3 Quarter annulus

The proposed TO method is used to optimize a quarter annulus with inner radius $R_{in} = 1.00$ and outer radius $R_{out} = 2.00$ as shown in Fig. 15a. The bottom edge is fixed and a concentrated force is horizontally loaded at left-top corner. The volume ratio is set to 0.5. The equal-interval initial holes are distributed in the design domain as shown in Fig. 15b.

A mesh of 64×64 elements is for design domain during the TO of the quarter annulus, and different stages of the opti-

Fig. 12 The design domain and the initial holes of the Michell type structure: **a** design domain and **b** distribution of initial holes

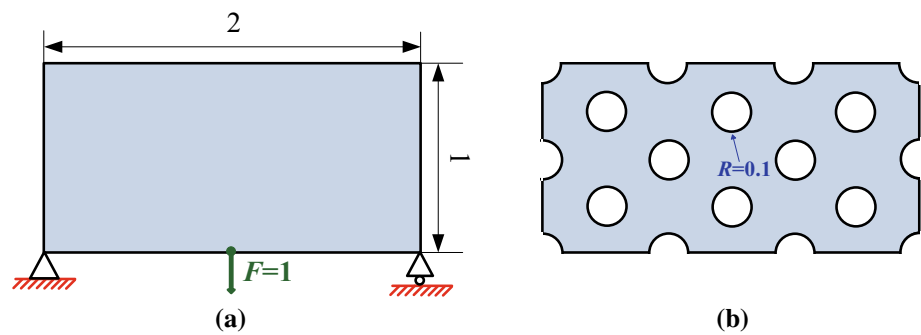


Fig. 13 Optimization stages of the Michell type structure: **a** initial design, **b** stage 2, **c** stage 4, **d** stage 10, **e** stage 20 and **f** stage 46 (Final result)

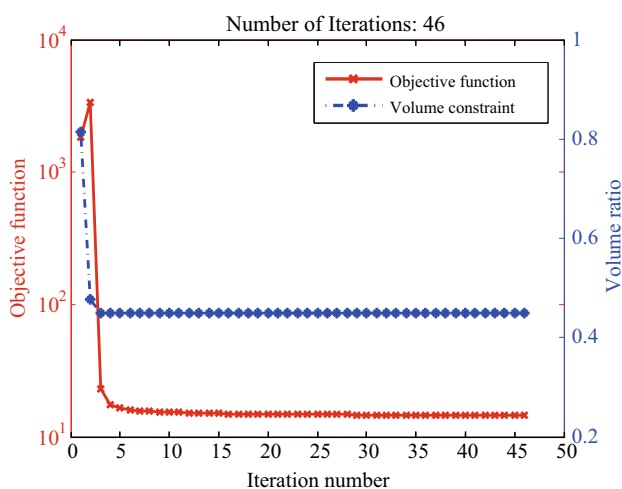
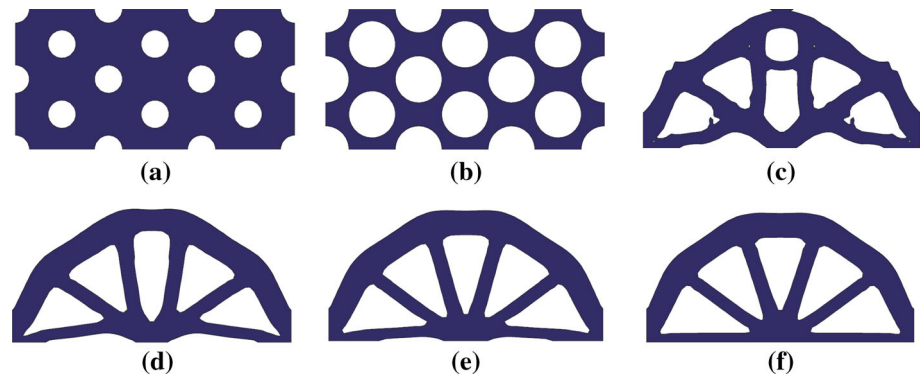


Fig. 14 Convergent histories of the Michell type structure

mization process are shown in Fig. 16. The structure evolves in a manner similar to the Michell problem shown in Fig. 13: the structure changes rapidly during the initial iterations and most of the later iterations adjust the geometric details. Note that no spatial discretization error exists here although some boundaries of the design domain are curves. The objective function and the volume ratio over the iterations are given in Fig. 17.

Similar to Fig. 14, the objective function values are very large at the beginning of the optimization (see Fig. 17), but the reason for this is that the force, and not a constraint, is applied at a point inside the initial hole (see the left-top cor-

ner in Fig. 16a), which results in a large strain energy. During the TO, the left-top corner is rapidly filled with solid material in stage 2 (see Fig. 16b) and the objective function value decreases to a normal value, and we take this objective function value 138.84 as a reference. The objective function value decreases from 138.84 to 72.00 after 144 iterations demonstrating the rapid convergence of the proposed method. The objective functions of iteration 10 and 70 are 84.29 and 73.33, respectively. The percentage decrease of the objective function of iterations 1–10, 11–70 and 71–144 are 81.6, 16.4 and 2.0 %, respectively, which demonstrates that the geometry of the structure changes rapidly at the beginning and then slows.

6 Conclusions

With the conventional FEM-based TO, higher order elements have high accuracy and rapid convergence, but their cost is high. Topology optimization with higher order elements has therefore not been with industry despite its theoretical attractions. IGA, which directly uses exact geometry in the analysis, avoids the spatial discretization error of the conventional FEM, and greatly improves the efficiency of computation with high-order elements [28]. Therefore, using IGA to replace the conventional FEM in the TO may be a key ingredient for TO with high efficiency and accuracy.

In this paper, IGA is first introduced into the parameterized LSM-based TO, and the proposed isogeometric LSM-based

Fig. 15 Design domain and initial holes of the quarter annulus: **a** design domain and **b** distribution of initial holes

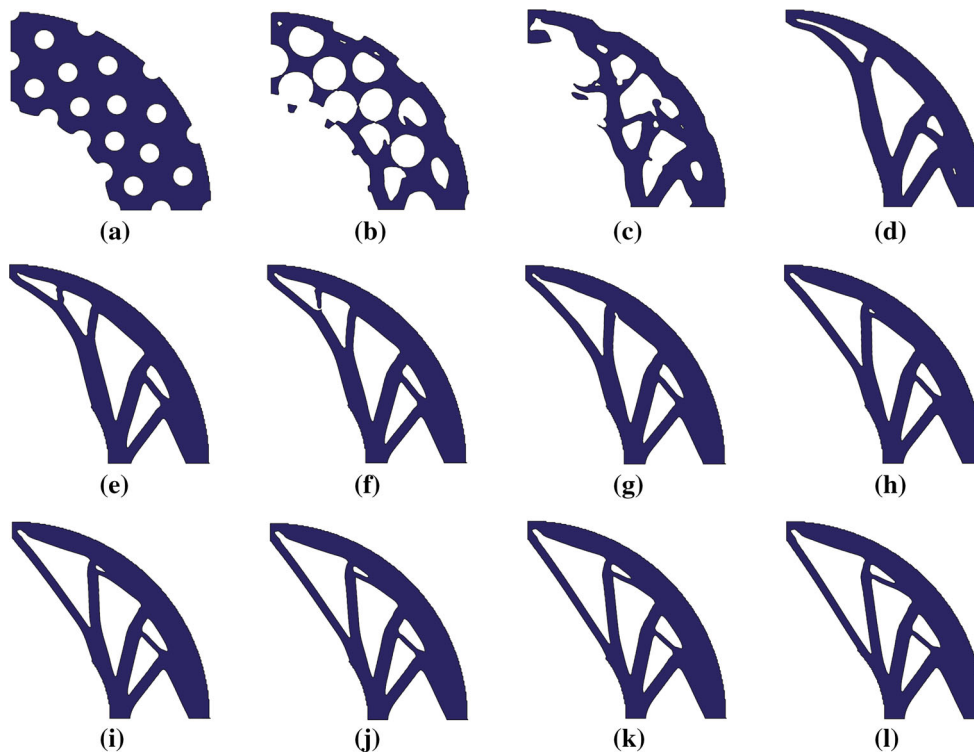
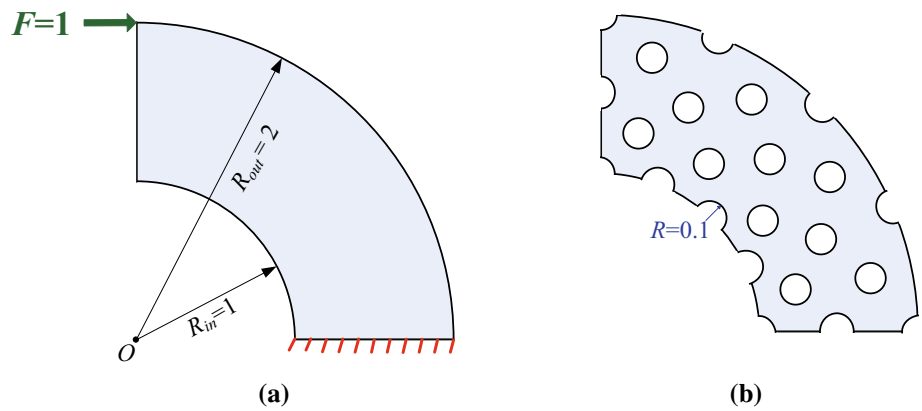


Fig. 16 Optimization stages of the quarter annulus: **a** initial design, **b** stage 2, **c** stage 4, **d** stage 10, **e** stage 20, **f** stage 30, **g** stage 40, **h** stage 70, **i** stage 90, **j** stage 100 and **f** stage 144 (Final result)

TO has the advantages of both the parameterized LSM and IGA. A collocation point scheme based on Greville abscissae is proposed for the LSF construction, and an interpolation point scheme using the vertices of the spans is adopted for the area computation and the visualization. Both the LSF parameterization and the isogeometric computation are using the same NURBS basis functions. Besides that, the isogeometric computation using the “ersatz material” approach is presented so that the mesh regeneration is successfully avoided.

Through the benchmark numerical example of the cantilever beam, we analyzed the influence of the initial holes, and verified the high efficiency of the isogeometric parame-

terized LSM-based TO by comparing it to the conventional parameterized LSM-based TO. A Michell structure example was used to further demonstrate the effectiveness of the proposed method. Moreover, a quarter annulus example with curve boundaries demonstrates that the proposed isogeometric TO method can directly use the exact CAD model without spatial discretization error.

Future research will focus on better methods for imposing Dirichlet boundary conditions, e.g. Nitsche’s method [22], to deal with the inaccurate loading problems, and improved quadrature for IGA [30] for higher efficiency and accuracy. To further improve the accuracy, optimal quadrature for arbitrary shapes and topology [44] may replace the density-based

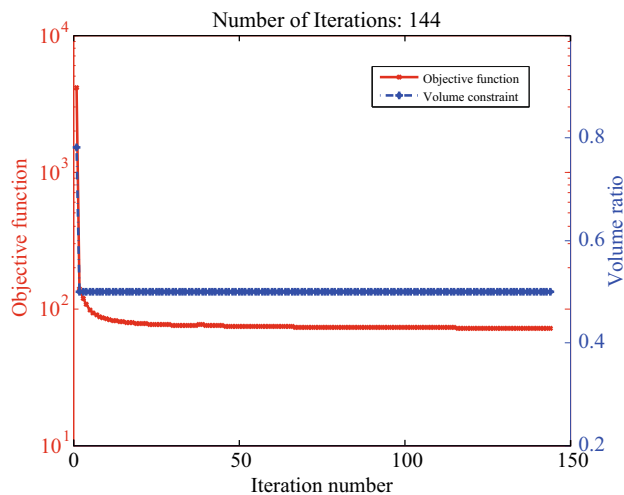


Fig. 17 Convergent histories of the quarter annulus

approach in the stiffness matrix computation of the elements trimmed by the zero level set. Moreover, expanding the proposed TO method to 3D problems is also a high research priority.

Acknowledgments The support for this research and Yingjun Wang by NSF grant CMMI-1068106 is gratefully acknowledged.

References

- Allaire G, Bonnetier E, Francfort G, Jouve F (1997) Shape optimization by the homogenization method. *Numer Math* 76(1):27–68
- Allaire G, De Gournay F, Jouve F, Toader AM (2005) Structural optimization using topological and shape sensitivity via a level set method. *Control Cybern* 34:59–80
- Allaire G, Jouve F, Toader AM (2002) A level-set method for shape optimization. *CR Math* 334(12):1125–1130
- Allaire G, Jouve F, Toader AM (2004) Structural optimization using sensitivity analysis and a level-set method. *J Comput Phys* 194(1):363–393
- Augier B, Yan J, Korobenko A, Czarnowski J, Ketterman G, Bazilevs Y (2014) Experimental and numerical FSI study of compliant hydrofoils. *Comput Mech* 55(6):1079–1090
- Azegami H, Fukumoto S, Aoyama T (2013) Shape optimization of continua using NURBS as basis functions. *Struct Multidiscip Optim* 47(2):247–258
- Bazilevs Y, Hsu MC, Scott MA (2012) Isogeometric fluid-structure interaction analysis with emphasis on non-matching discretizations, and with application to wind turbines. *Comput Methods Appl Mech Eng* 249:28–41
- Bazilevs Y, Takizawa K, Tezduyar TE, Hsu MC, Kostov N, McIntyre S (2014) Aerodynamic and FSI analysis of wind turbines with the ALE-VMS and ST-VMS methods. *Arch Comput Methods Eng* 21:1–40
- Bendsøe MP (1989) Optimal shape design as a material distribution problem. *Struct Optim* 1(4):193–202
- Bendsøe MP, Kikuchi N (1988) Generating optimal topologies in structural design using a homogenization method. *Comput Methods Appl Mech Eng* 71(2):197–224
- Bendsøe MP, Sigmund O (2003) *Topology optimization: theory, methods and applications*. Springer, New York
- Benson DJ, Bazilevs Y, Hsu M-C, Hughes TJR (2011) A large deformation, rotation-free, isogeometric shell. *Comput Methods Appl Mech Eng* 200:1367–1378
- Benson DJ, Hartmann S, Bazilevs Y, Hsu M-C, Hughes TJR (2013) Blended isogeometric shells. *Comput Methods Appl Mech Eng* 255:133–146
- De Boor C (1972) On calculating with B-splines. *J Approx Theory* 6(1):50–62
- De Boor C, Swartz B (1973) Collocation at gaussian points. *SIAM J Numer Anal* 10(4):582–606
- Borrvall T, Petersson J (2003) Topology optimization of fluids in stokes flow. *Int J Numer Methods Fluids* 41(1):77–107
- Chen J, Freytag M, Shapiro V (2008) Shape sensitivity of constructively represented geometric models. *Comput Aided Geom Des* 25(7):470–488
- Chen J, Shapiro V, Suresh K, Tsukanov I (2007) Shape optimization with topological changes and parametric control. *Int J Numer Methods Eng* 71(3):313–346
- Cottrell JA, Hughes TJR, Bazilevs Y (2009) *Isogeometric analysis: toward integration of CAD and FEA*. Wiley, Chichester
- Deaton JD, Grandhi RV (2014) A survey of structural and multidisciplinary continuum topology optimization: post 2000. *Struct Multidiscip Optim* 49(1):1–38
- Dedè L, Borden MJ, Hughes TJR (2012) Isogeometric analysis for topology optimization with a phase field model. *Arch Comput Methods Eng* 19(3):427–465
- Embar A, Dolbow J, Harari I (2010) Imposing Dirichlet boundary conditions with Nitsche’s method and spline-based finite elements. *Int J Numer Meth Eng* 83(7):877–898
- Fedkiw S, Osher R (2003) *Level set methods and dynamic implicit surfaces*. Springer, New York
- Gersborg-Hansen A, Bendsøe MP, Sigmund O (2006) Topology optimization of heat conduction problems using the finite volume method. *Struct Multidiscip Optim* 31(4):251–259
- Hassani B, Hinton E (1998) A review of homogenization and topology optimization III: topology optimization using optimality criteria. *Comput Struct* 69(6):739–756
- Hsu MC, Bazilevs Y (2012) Fluid-structure interaction modeling of wind turbines: simulating the full machine. *Comput Mech* 50(6):821–833
- Hsu MS, Kamensky D, Xu F, Kiendl J, Wang C, Wu MCH, Mineroff J, Reali A, Bazilevs Y, Sacks MS (2015) Dynamic and fluid-structure interaction simulations of bioprosthetic heart valves using parametric design with T-splines and Fung-type material models. *Comput Mech* 55(6):1211–1225
- Hughes TJR, Cottrell JA, Bazilevs Y (2005) Isogeometric analysis: CAD, finite elements, NURBS, exact geometry, and mesh refinement. *Comput Methods Appl Mech Eng* 194:4135–4195
- Hughes TJR (2000) *The finite element method: linear static and dynamic finite element analysis*. Courier Dover Publications, Englewood Cliffs
- Hughes TJR, Reali A, Sangalli G (2010) Efficient quadrature for NURBS-based isogeometric analysis. *Comput Methods Appl Mech Eng* 199(5):301–313
- Jog CS, Haber RB (1996) Stability of finite element models for distributed-parameter optimization and topology design. *Comput Methods Appl Mech Eng* 130(3):203–226
- Johnson RW (2005) Higher order b-spline collocation at the greville abscissae. *Appl Numer Math* 52(1):63–75
- Kim HJ, Seo YD, Youn SK (2009) Isogeometric analysis for trimmed CAD surfaces. *Comput Methods Appl Mech Eng* 198(37):2982–2995
- Kumar A, Parthasarathy A (2011) Topology optimization using B-spline finite element. *Struct Multidiscip Optim* 44(4):471–481

35. Kwok KY, Moser RD, Jiménez J (2001) A critical evaluation of the resolution properties of b-spline and compact finite difference methods. *J Comput Phys* 174(2):510–551
36. Li K, Qian XP (2011) Isogeometric analysis and shape optimization via boundary integral. *Comput Aided Des* 43(11):1427–1437
37. Liu T, Wang S, Li B, Gao L (2014) A level-set-based topology and shape optimization method for continuum structure under geometric constraints. *Struct Multidiscip Optim* 50(2):253–273
38. Luo Z, Tong L, Kang Z (2009) A level set method for structural shape and topology optimization using radial basis functions. *Comput Struct* 87(7):425–434
39. Luo Z, Tong L, Wang MY, Wang S (2007) Shape and topology optimization of compliant mechanisms using a parameterization level set method. *J Comput Phys* 227(1):680–705
40. Luo Z, Wang MY, Wang SY, Wei P (2008) A level-set-based parameterization method for structural shape and topology optimization. *Int J Numer Meth Eng* 76(01):1–26
41. Maeda Y, Nishiwaki S, Izui K, Yoshimura M, Matsui K, Terada K (2006) Structural topology optimization of vibrating structures with specified eigenfrequencies and eigenmode shapes. *Int J Numer Methods Eng* 67(5):597–628
42. Mei Y, Wang X, Cheng G (2008) A feature-based topological optimization for structure design. *Adv Eng Softw* 39(2):71–87
43. Nagy AP, Abdalla MM, Gurdal Z (2010) Isogeometric sizing and shape optimization of beam structures. *Comput Methods Appl Mech Eng* 199:1216–1230
44. Nagy AP, Benson DJ (2015) On the numerical integration of trimmed isogeometric elements. *Comput Methods Appl Mech Eng* 284:165–185
45. Nagy AP, IJsselmuiden ST, Abdalla MM (2013) Isogeometric design of anisotropic shells: optimal form and material distribution. *Comput Methods Appl Mech Eng* 264:145–162
46. Osher S, Fedkiw RP (2001) Level set methods: an overview and some recent results. *J Comput Phys* 169(2):463–502
47. Osher S, Sethian JA (1988) Fronts propagating with curvature-dependent speed: algorithms based on Hamilton–Jacobi formulations. *J Comput Phys* 79(1):12–49
48. Piegl L, Tiller W (1997) *The NURBS book* (monographs in visual communication). Springer, New York
49. Press WH, Teukolsky SA, Vetterling WT, Flannery BP (2007) *Numerical recipes, 3rd edn, The art of scientific computing*. Cambridge university press, Cambridge
50. Qian XP (2010) Full analytical sensitivities in NURBS based isogeometric shape optimization. *Comput Methods Appl Mech Eng* 199(29):2059–2071
51. Qian XP (2013) Topology optimization in B-spline space. *Comput Methods Appl Mech Eng* 265:15–35
52. Rozvany GIN, Zhou M, Birker T (1992) Generalized shape optimization without homogenization. *Struct Optim* 4(3–4):250–252
53. Seo YD, Kim HJ, Youn SK (2010) Isogeometric topology optimization using trimmed spline surfaces. *Comput Methods Appl Mech Eng* 199(49):3270–3296
54. Seo YK, Kim HJ, Youn SK (2010) Shape optimization and its extension to topological design based on isogeometric analysis. *Int J Solids Struct* 47(11):1618–1640
55. Sethian JA, Wiegmann A (2000) Structural boundary design via level set and immersed interface methods. *J Comput Phys* 163(2):489–528
56. Sigmund O (2001) Design of multiphysics actuators using topology optimization-Part I: one-material structures. *Comput Methods Appl Mech Eng* 190(49):6577–6604
57. Sigmund O, Petersson J (1998) Numerical instabilities in topology optimization: a survey on procedures dealing with checkerboards, mesh-dependencies and local minima. *Struct Optim* 16(1):68–75
58. Sigmund Ole (2001) A 99 line topology optimization code written in matlab. *Struct Multidiscip Optim* 21(2):120–127
59. Suzuki K, Kikuchi N (1991) A homogenization method for shape and topology optimization. *Comput Methods Appl Mech Eng* 93(3):291–318
60. van Dijk NP, Maute K, Langelaar M, Van Keulen F (2013) Level-set methods for structural topology optimization: a review. *Struct Multidiscip Optim* 48(3):437–472
61. Wang MY, Wang X (2004) Pde-driven level sets, shape sensitivity and curvature flow for structural topology optimization. *Comput Model Eng Sci* 6:373–396
62. Wang MY, Wang X, Guo D (2003) A level set method for structural topology optimization. *Comput Methods Appl Mech Eng* 192(1):227–246
63. Wang S, Wang MY (2006) Radial basis functions and level set method for structural topology optimization. *Int J Numer Methods Eng* 65(12):2060–2090
64. Wang SY, Lim KM, Khoo BC, Wang MY (2007) An extended level set method for shape and topology optimization. *J Comput Phys* 221(1):395–421
65. Wang SY, Tai K (2004) Graph representation for structural topology optimization using genetic algorithms. *Comput Struct* 82(20):1609–1622
66. Wang SY, Wang MY (2006) Structural shape and topology optimization using an implicit free boundary parametrization method. *Comput Model Eng Sci* 13(2):119
67. Wang YJ, Benson DJ (2015) Multi-patch nonsingular isogeometric boundary element analysis in 3d. *Comput Methods Appl Mech Eng* 293:71–91
68. Wang YJ, Benson DJ, Nagy AP (2015) A multi-patch nonsingular isogeometric boundary element method using trimmed elements. *Comput Mech* 56(1):173–191
69. Wei P, Wang MY, Xing X (2010) A study on x-fem in continuum structural optimization using a level set model. *Comput Aided Des* 42(8):708–719
70. Xie YM, Steven GP (1993) A simple evolutionary procedure for structural optimization. *Comput Struct* 49(5):885–896
71. Zhou M, Rozvany GIN (1991) The coc algorithm, Part II: topological, geometrical and generalized shape optimization. *Comput Methods Appl Mech Eng* 89(1):309–336
72. Zhou S, Li W, Li Q (2010) Level-set based topology optimization for electromagnetic dipole antenna design. *J Comput Phys* 229(19):6915–6930